PHOTONICS Research

Graphitic carbon nitride, a saturable absorber material for the visible waveband

Mengxia Wang,[1,†] Fukun Ma,[1,†] Zhengping Wang,[1,*] Dawei Hu,[2] Xinguang Xu,[1] and Xiaopeng Hao[1,3]

[1]State Key Laboratory of Crystal Materials, Shandong University, Jinan 250100, China
[2]Research Institute of Science and Technology, Shandong University, Jinan 250100, China
[3]e-mail: xphao@sdu.edu.cn
*Corresponding author: zpwang@sdu.edu.cn

Received 9 November 2017; revised 25 January 2018; accepted 30 January 2018; posted 1 February 2018 (Doc. ID 313152); published 27 March 2018

For the first time to our knowledge, graphitic carbon nitride (g-C_3N_4) nanosheets are found to be an excellent saturable absorber material in the visible waveband. g-C_3N_4 exhibits much stronger saturable absorption in this region than in the near-infrared region, unlike other two-dimensional materials such as graphene and black phosphorus. By the Z-scan method, the nonlinear absorption coefficient β of the material is first measured at three visible wavelengths, and for g-C_3N_4 it is −2.05, −0.34, and −0.11 cm · GW^{-1} at 355, 532, and 650 nm, respectively. These are much larger than −0.06 cm · GW^{-1} at 1064 nm.

OCIS codes: (160.4330) Nonlinear optical materials; (160.4236) Nanomaterials; (190.4400) Nonlinear optics, materials.

https://doi.org/10.1364/PRJ.6.000307

1. INTRODUCTION

The exploration of new two-dimensional (2D) materials, such as graphene [1–3], topological insulators [4], and transition-metal dichalcogenides [5] has attracted wide attention in recent years because of their exceptional chemical and physical properties. These layered materials exhibit a common characteristic of possessing strong atomic forces between the atoms within a layer and weak van der Waals forces between adjacent atomic layers. This results in their special electronic and optoelectronic properties. Because of the large nonlinear optical (NLO) susceptibility, high carrier density, and mobility, they have been utilized as multiple optical components such as passive saturable absorbers for *Q*-switching and mode-locking, optical limiters, and photodetectors [6–12].

Graphitic carbon nitride (g-C_3N_4), a metal-free 2D conjugated semiconductor, has attracted research attention since 2009 because of its sustainable photocatalytic ability [13,14]. g-C_3N_4 possesses highly stable chemical, thermal, and photochemical properties for its tri-s-triazine ring structure and a high degree of polymerization [13]; therefore it can be used in photocurrent, photoreactivity, electrocatalysis, and bioimaging applications [13,15,16]. Compared with the chemical properties, the optical characteristics of g-C_3N_4 have received less attention. In the last two years, due to the saturable absorption (SA) property of g-C_3N_4, researchers have realized its applications in passive *Q*-switching and mode-locking of infrared lasers at wavelengths 1, 1.3, 2.84, and 2.95 μm [17–20]. However, SA in the visible waveband has never been observed for pure g-C_3N_4 [21,22].

In this study, we used the Z-scan method to investigate the NLO properties of g-C_3N_4 at different wavelengths, with picosecond laser pulses as the excitation source. For the first time to our knowledge, strong SA was observed in a g-C_3N_4 dispersion in the visible waveband. At the same time, under long wavelength (650 and 1064 nm) excitation, two opposite absorption phenomena, namely, SA and optical limiting (OL), were found when we changed the input intensity. The nonlinear absorption coefficient β and the nonlinear refractive index n_2 were calculated from the experimental results of open aperture (OA) and closed aperture (CA) Z-scan measurements. For a g-C_3N_4 dispersion with 60% initial transmittance, the β values are −2.05, −0.34, −0.11, and −0.06 cm · GW^{-1} at 355, 532, 650, and 1064 nm, respectively. This illustrates that the SA ability of g-C_3N_4 is stronger at shorter wavelengths. Currently, diode-pumped continuous-wave visible solid-state lasers that can generate various colors are undergoing rapid development [23]. By directly inserting nanomaterial produced saturable absorbers, such as Au nanorods, MoS_2, or Bi_2Se_3, visible laser pulses can be obtained conveniently [24–26]. Besides, 2D nanomaterials have also been applied to the passive *Q*-switching of visible fiber lasers [27,28]. As a new, powerful SA material, g-C_3N_4 is hoped to produce pulsed visible lasers with the advantages of high efficiency, affordability, and compactness with potential applications in medical treatment, material processing, microscopy, and scientific research, etc.

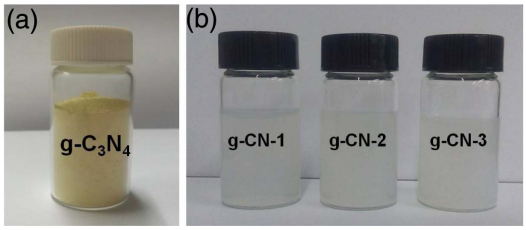

Fig. 1. Photographs of (a) g-C_3N_4 powder and (b) prepared g-C_3N_4 dispersions.

2. EXPERIMENT

A. Sample Preparation

Bulk g-C_3N_4 was synthesized by direct heating of dicyandiamide [29]. First, dicyandiamide was heated at 550°C for 4 h in static air at a ramp rate of 2.3°C/min. Then, it was cooled down to the room temperature at a cooling rate of 1°C/min. The resultant yellow agglomerate was finely ground to powder, as shown in Fig. 1(a).

The g-C_3N_4 dispersion was prepared by the liquid exfoliation method. The as-obtained powder was dispersed in deionized water with ultrasonic pulverization for 2 h. Then the suspension was allowed to settle for two days to deposit the undispersed particles. The final supernatant g-C_3N_4 dispersion was used in the Z-scan experiment. The g-CN-1, g-CN-2, and g-CN-3 samples [as shown in Fig. 1(b)] had different g-C_3N_4 contents, and their linear optical transmittances at 532 nm were 75%, 60%, and 43.5%, respectively. The samples prepared were stable and could be stored without any change in appearance for more than one month. This feature makes them suitable for time-consuming measurements and is also advantageous for future applications.

B. Characterization

Atomic force microscopy (AFM) and X-ray diffraction (XRD) were used to analyze the morphology and structure of the g-C_3N_4 sample. Before the AFM measurement, the sample was deposited on a Si/SiO_2 substrate and dried for 12 h. As shown in Fig. 2, the thickness of the g-C_3N_4 nanosheets is about 4–6 nm. Assuming an interplanar stacking distance of 0.326 nm [30] for the aromatic units, this thickness corresponds to a packing of 12–18 layers.

The XRD result was obtained on a Bruker D8 advance X-ray diffractometer under Cu–Kα radiation ($\lambda = 0.15418$ nm). As presented in Fig. 3, there are two primary diffraction peaks located at 13.1° and 27.6°. The (100) peak at 13.1° reveals

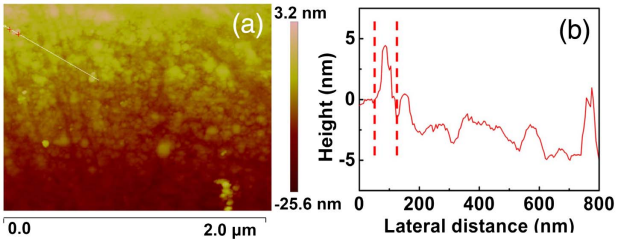

Fig. 2. (a) AFM image and (b) corresponding height profile of prepared g-C_3N_4 nanosheets.

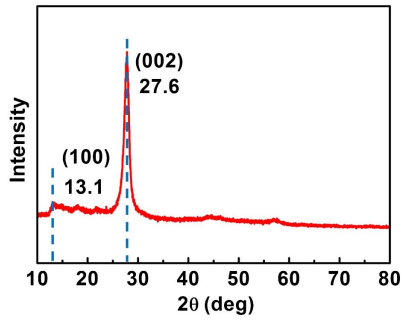

Fig. 3. XRD pattern of g-C_3N_4 nanosheets.

the in-plane structural packing motif, and the (002) peak at 27.6° shows typical graphite-like stacking of the conjugated aromatic C-N segments [30,31]. The result reflects the graphite-like structure of the g-C_3N_4 powder and confirms that the influence of amino on the structure of g-C_3N_4 can be neglected.

Using 1064 nm light as the excitation source, the Raman spectrum of g-C_3N_4 powder was recorded. As shown in Fig. 4, the peak at 707 cm^{-1} attributes to the heptazine ring breathing mode. The peaks around 1232 cm^{-1} correspond to the stretching vibration mode of C-N heterocycles [32]. The 1566 cm^{-1} fingerprint peak of the NH_2 bending mode does not appear, which proves the high purity of the g-C_3N_4 powder.

Figure 5(a) shows the transmission spectrum of the g-C_3N_4-2 sample in the range of 250–1750 nm. It can be seen that the ultraviolet (UV) absorption cutting edge of g-C_3N_4 is shorter than 250 nm. The UV absorption peak at 300 nm is

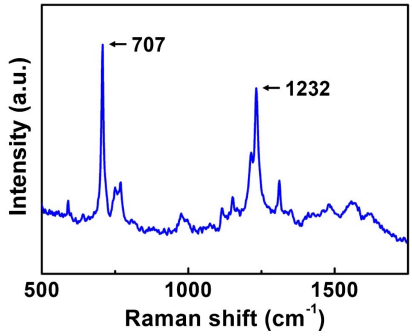

Fig. 4. Raman spectrum of g-C_3N_4 powder.

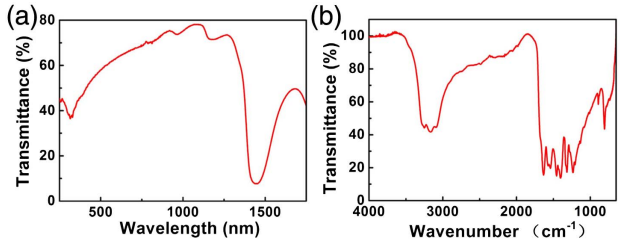

Fig. 5. Transmission characteristic of g-C_3N_4. (a) UV–near infrared spectrum from 250 to 1750 nm. (b) FTIR spectrum from 2.5 to 15.4 μm (4000 – 650 cm^{-1}).

due to the π bond transition of g-C_3N_4. The absorption bands around 965, 1180, and 1450 nm are attributed to the O—H bond vibrations of water in g-C_3N_4 dispersion. Figure 5(b) is the Fourier transform infrared (FTIR) transmission spectrum of g-C_3N_4 powder in the range of 2.5–15.4 μm measured with a Perkin Elemer 100 FTIR spectrophotometer. In the infrared direction, the cutting edge extends beyond 15.4 μm (650 cm^{-1}). This result means that a wide waveband from visible to infrared is available for optical applications. The broad absorption band from 3000 to 3300 cm^{-1} originates from the stretching vibration of the N—H bond, associated with uncondensed amino groups [33]. The other broad absorption bands in the 1200–1600 cm^{-1} region are assigned to the typical stretching vibration modes of C-N heterocycles. The sharp peak at 810 cm^{-1} attributes to the breathing vibration of triazine units [34,35].

3. NONLINEAR OPTICAL MEASUREMENT

The Z-scan method is a popular technique for characterizing the NLO properties of materials, including nonlinear absorption, scattering, and refraction [36]. Based on different materials and absorption mechanisms, the nonlinear absorption can be multiphoton absorption, reverse saturable absorption (RSA), and free-carrier absorption, etc. In this study, a Z-scan apparatus was used to study the NLO behavior of g-C_3N_4 dispersions at four wavelengths, namely, 355, 532, 650, and 1064 nm.

The experimental setup is shown in Fig. 6. The fundamental light source is a mode-locked Nd:YAG dye laser (PY61C-10, Continuum Inc, USA), which can operate at a near-infrared wavelength of 1064 nm. After frequency doubling and third harmonic generation with NLO crystals, 532 nm and 355 nm excitation wavelengths can be obtained. Further, after stimulated Raman scattering of pure water to the 532 nm output, the 650 nm excitation wavelength is obtained. Thus four representative wavelengths, namely, deep violet (355 nm), green (532 nm), red (650 nm), and near infrared (1064 nm), can be used for the Z-scan experiments. The pulse widths are 20, 30, 35, and 40 ps for 355, 532, 650, and 1064 nm, respectively. The pulse repetition rate is 10 Hz. The focal length of the focusing lens is 40 cm. The experimental samples, i.e., the g-C_3N_4 dispersions with different concentrations, were transferred to quartz cuvettes of 1 mm thickness. During the experiments, each Z-scan for the g-C_3N_4 dispersions was companied by a reference scan for the quartz substrate with deionized water. The final Z-scan results were obtained by dividing the g-C_3N_4 data by the quartz substrate with deionized water data. In this way, the thermal effects, nonlinear effects from the quartz substrate, and the deionized water were removed.

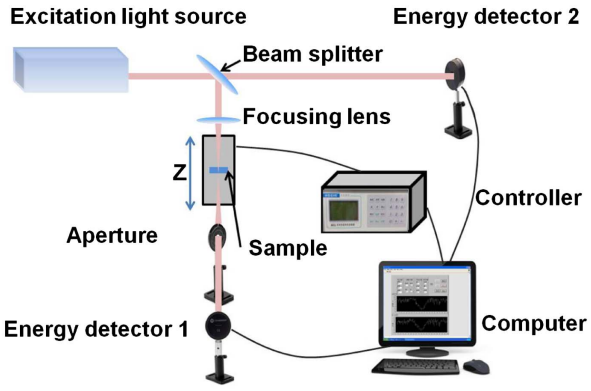

Fig. 6. Schematic of the Z-scan experimental setup.

Figure 7 presents the OA Z-scan results of g-C_3N_4 dispersions (g-C_3N_4-1, g-C_3N_4-2, and g-C_3N_4-3) at the excitation wavelengths of 355, 532, 650, and 1064 nm. The linear optical transmission values of g-C_3N_4-1, g-C_3N_4-2, and g-C_3N_4-3 are 55%, 43.6%, and 30% at 355 nm; 75%, 60%, and 43.5% at 532 nm; 81.8%, 65.5%, and 50% at 650 nm; and 82.4%, 73.5%, and 65% at 1064 nm, respectively.

Figures 7(a)–7(d) show the variation of normalized transmission as a function of the incident pulse energy density ($J \cdot cm^{-2}$) for different g-C_3N_4 samples. All samples exhibit a gradual increase in the transmittance with increasing incident energy at 355 and 532 nm, indicating typical SA. This is the first time that SA is observed in the visible waveband for g-C_3N_4. Furthermore, for the same sample, the strongest SA response is seen at the shortest excitation wavelength, 355 nm. Normalized transmittance T_N is used to scale the output

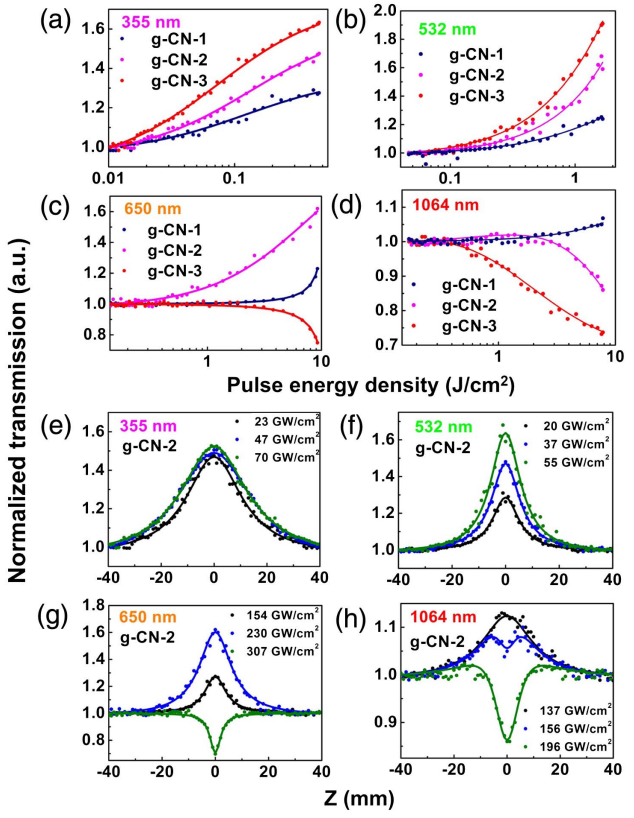

Fig. 7. OA Z-scan results of g-C_3N_4 nanosheets. (a) Different g-C_3N_4 samples at 355 nm. (b) Different g-C_3N_4 samples at 532 nm. (c) Different g-C_3N_4 samples at 650 nm. (d) Different g-C_3N_4 samples at 1064 nm. (e) g-C_3N_4-2 sample at different 355 nm excitation intensities. (f) g-C_3N_4-2 sample at different 532 nm excitation intensities. (g) g-C_3N_4-2 sample at different 650 nm excitation intensities. (h) g-C_3N_4-2 sample at different 1064 nm excitation intensities.

clamping characteristics of different g-C_3N_4 samples. A larger T_N implies better SA. When the 355 nm input fluence at the focal point ($Z = 0$) is fixed at 0.47 J · cm^{-2} (corresponding to an intensity of 23 GW · cm^{-2}), the T_N values of g-C_3N_4-1, g-C_3N_4-2, and g-C_3N_4-3 samples can reach 128%, 147%, and 162%, respectively. This indicates that the SA ability increases with decreasing linear optical transmission. Under the same experimental conditions, the T_N value of black phosphorus can only reach 115% at a much higher incident intensity of 115 GW · cm^{-2}. For 532 nm excitation, contrary to earlier reports on OL phenomena [21,22], all of the three g-C_3N_4 samples exhibit the SA effect under picosecond pulses. When the input fluence at the focal point is fixed at 1.66 J · cm^{-2} (corresponding to an intensity of 55 GW · cm^{-2}), the T_N values of g-C_3N_4-1, g-C_3N_4-2, and g-C_3N_4-3 samples are 125%, 163%, and 192%, respectively. Similarly, for 355 nm excitation, the SA ability increases with decreasing linear optical transmission. At 650 nm, the g-C_3N_4 dispersions exhibit two opposite NLO phenomena, SA and OL. When the input fluence at the focal point is fixed at 9.23 J · cm^{-2} (corresponding to an intensity of 230 GW · cm^{-2}), the T_N values of g-C_3N_4-1, g-C_3N_4-2, and g-C_3N_4-3 samples are 123%, 160%, and 75%, respectively. With decreasing linear optical transmission, the NLO responses of g-C_3N_4 dispersions shift from SA to OL. This means that the nonlinear absorption parameters of the g-C_3N_4 nanosheets have changed significantly with the changing initial linear optical transmission, or in other words, the concentration of the g-C_3N_4 dispersion. Meanwhile, at the wavelength of 1064 nm, no obvious SA behavior is shown by the three g-C_3N_4 dispersions. After increasing the fluence of the 1064 nm laser to 7.83 J · cm^{-2}, the samples show two different NLO phenomena, namely, weak SA and strong RSA. The T_N values of g-C_3N_4-1, g-C_3N_4-2, and g-C_3N_4-3 are 105%, 86%, and 74%, respectively. Furthermore, the NLO absorption properties of g-C_3N_4 shift from SA to RSA with decreasing initial transmission. Such behavior indicates that g-C_3N_4 is highly suitable for the protection of infrared lasers. Overall, with increasing concentration, the g-C_3N_4 dispersion shows a lower initial linear transmittance, larger transmission variation magnitude, and more significant NLO absorption. Therefore, the g-C_3N_4-3 sample shows the strongest SA effect at low excitation energy densities (355 and 532 nm) and the strongest RSA effect at high excitation energy densities (650 and 1064 nm). As a layered material, g-C_3N_4 is based on tri-s-triazine building blocks, and the van der Waals forces between each layer lead to the π–π stacking [17]. It possesses higher charge carrier density due to an obvious increase of state density at the conduction band edge with respect to the bulk counterpart [37]. Its SA feature comes from the Pauli blocking effect of the conduction band and the depletion of the valence electrons under intense laser field.

Figures 7(e)–7(h) present the OA Z-scan results of the g-C_3N_4-2 sample at different excitation wavelengths and different energy intensities. At 355 nm, the values of T_N are 147%, 149%, and 152% for the energy intensities ($Z = 0$) of 23, 47, and 70 GW · cm^{-2}, respectively. At 532 nm, the T_N values are 128%, 147%, and 163% when the energy intensities are 20, 37, and 55 GW · cm^{-2}, respectively. It can be seen that at these two wavelengths the SA ability of g-C_3N_4 dispersion grows with increasing incident intensity. Under the excitation of 650 and 1064 nm lasers, the g-C_3N_4-2 dispersion exhibits SA and OL behaviors at different incident intensities. Therefore, in the near-infrared waveband, g-C_3N_4 can serve as an optical modulation material depending on the practical working conditions. From the excited state nonlinear absorption theory [38,39], it can be known that at 355 and 532 nm, $\sigma_1 > \sigma_2$ for g-C_3N_4-2, where σ_1 and σ_2 are the absorption cross sections of the first and the second excited states, respectively. Under such conditions, only the SA effect occurs [Figs. 7(e) and 6(f)]. At 650 and 1064 nm, $\sigma_1 < \sigma_2$. Under this condition, the SA effect will change to the RSA effect when the incident intensity reaches a certain threshold, which is inversely proportional to the value of $\sigma_2 - \sigma_1$. Figure 5(a) reveals that for g-C_3N_4-2, σ_1 (650 nm) > σ_1 (1064 nm), so if σ_2 is assumed to be unchanged from 650 to 1064 nm, then $\sigma_2 - \sigma_1$ at 650 nm will be smaller than that at 1064 nm and correspondingly the SA → RSA inversion intensity threshold at 650 nm will be larger. This is in accordance with the experimental phenomena: the inversion threshold at 650 nm is larger than 230 GW · cm^{-2} [Fig. 7(g)], while the one at 1064 nm is between 137 and 156 GW · cm^{-2} [Fig. 7(f)].

The normalized transmittance for the OA Z-scan experiment can be expressed as [36]

$$T_{\mathrm{OA}}(z) = \sum_{m=0}^{\infty} \frac{[-q_0(z,0)]^m}{(m+1)^{1.5}},\ m \in N, \tag{1}$$

$$q_0(z,0) = \frac{\beta I_0 L_{\mathrm{eff}}}{1 + z^2/z_R^2}, \tag{2}$$

where β is the nonlinear absorption coefficient, I_0 is the peak intensity at the focus point ($z = 0$), $L_{\mathrm{eff}} = (1 - e^{-\alpha_0 L})/\alpha_0$ is the effective length, L is the length of the sample, α_0 is the linear absorption coefficient, z is the position of the sample, and z_R is the Rayleigh length.

Taking the g-C_3N_4-2 sample as an example, the value of the nonlinear absorption coefficient β is fitted to be (−2.05 ± 0.4) cm · GW^{-1} under different 355 nm intensities [Fig. 7(e)]. At 532 nm, the β value is fitted to be (−0.34 ± 0.02) cm · GW^{-1} under different 532 nm intensities [Fig. 7(f)]. For 650 nm, the β value is −0.11 cm · GW^{-1} at 230 GW · cm^{-2} and 0.014 cm · GW^{-1} at 307 GW · cm^{-2}. At 1064 nm excitation [Fig. 7(h)], the fitted β value is −0.06 cm · GW^{-1} at 137 GW · cm^{-2} and 0.016 cm · GW^{-1} at 196 GW · cm^{-2}. The β values at all of the four wavelengths are listed in Table 1, as well as the corresponding saturation intensities I_s. I_s is defined as the optical intensity required to increase the saturable transmission to a half. For g-C_3N_4-2, the I_s values in Table 1 are obtained from Figs. 7(a)–7(c) and 7(h) (at 137 GW · cm^{-2}), respectively. Based on a 30 ps, 532 nm laser, the I_s of g-C_3N_4-2 is 11.4 GW · cm^{-2}, which is much larger than the values of graphene oxide (0.86 GW · cm^{-2}) [40], black phosphorus (7.6 MW · cm^{-2}) [41], and MoS_2 (1 GW · cm^{-2}) [42] under similar conditions. The large I_s represents high energy storage ability, which indicates that g-C_3N_4 will be a powerful Q-switcher material

Table 1. Nonlinear Optical Properties of g-C_3N_4-2 Sample at Different Visible Wavelengths

Wavelength/nm	I_s/GW · cm^{-2}	β/cm · GW^{-1}	n_2 /cm^2 · W^{-1}	Im$\chi^{(3)}$/esu	Re$\chi^{(3)}$/esu	FOM/m^4 · (sW)$^{-1}$
355	4.6	−2.05	0.87×10^{-15}	-4.00×10^{-12}	0.62×10^{-13}	2.19×10^{-22}
532	11.4	−0.34	1.42×10^{-15}	-6.62×10^{-13}	1.02×10^{-13}	5.44×10^{-23}
650	185	−0.11	0.40×10^{-15}	-4.03×10^{-13}	0.27×10^{-13}	1.69×10^{-23}
1064	60.3	−0.06	0.34×10^{-15}	-2.20×10^{-13}	0.23×10^{-13}	1.51×10^{-23}

Table 2. Nonlinear Absorption Properties of g-C_3N_4-2 Sample and Several Representative Nanomaterials at Visible Wavelength of 532 nm

Sample	Laser Pulse Duration/ps	I_0/GW · cm^{-2}	Main NLO Response/nm	β/cm · GW^{-1}	Reference
g-C_3N_4-2	30	20–55	SA	−0.34	This work
Graphene	30	12.8	RSA	0.4	[43]
Graphene oxide	35	0–34	RSA	2.2	[44]
	35	0–30	RSA	2.5	[40]
	35	20	RSA	2	[45]
BP	30	0.114	RSA	16	[41]
MoS_2	19	2.1	RSA	−0.0003–0.5	[42]
BCN	35	94	RSA	0.08–0.106	[46]
Carbon nanotubes	35	22	RSA	0–1	[44]

based on the theory of passively modulated pulsed lasers [47]. From Fig. 7(b), it can be known that g-C_3N_4-2 possesses a large saturable loss (36%) and a small non-saturable loss (4%). The other favorable characteristics includes short recovery time (4 ps) [48] and high laser damage threshold (>8 MW · cm^{-2} for mid-infrared solid-state laser Q-switching) [19].

At the same visible excitation wavelength of 532 nm, the nonlinear absorption properties of the g-C_3N_4-2 sample and several representative nanomaterials are compared in Table 2 [40–46]. It can be seen that at a similar laser pulse duration (~30 ps) and energy range of 10 – 100 GW · cm^{-2}, only g-C_3N_4-2 presents an SA response ($\beta < 0$). At the same time, compared with other popular 2D materials, such as graphene [49], black phosphorus (BP) [41], and boron carbon nitride (BCN) [46], g-C_3N_4 exhibits a different SA characteristic, i.e., a larger SA coefficient in the visible waveband (355, 532, and 650 nm) than in the infrared region (1064 nm). All of these properties indicate that g-C_3N_4 is a powerful 2D SA material in the visible waveband. In earlier reports, nanosecond lasers were used to study the NLO effects of g-C_3N_4 at 532 nm. No NLO response was observed under a power intensity of 0.8 GW · cm^{-2}, and the OL effect was observed under a power intensity of 4 GW · cm^{-2} [21,22]. We used picosecond lasers as the excitation light source; they can supply a much higher power intensity than what was produced from the nanosecond lasers in earlier works. Thus, the SA effect is easier to realize. Besides, the dispersion concentration has a positive influence on the NLO performance; the NLO phenomena are more remarkable at higher dispersion concentrations.

The nonlinear refractive index can be extracted by dividing the CA data by the OA data. The results are shown in Fig. 8. The valley-peak configurations reveal that the nonlinear refractive index is positive, which shows that self-focusing occurs in g-C_3N_4 dispersions when they are irradiated by high power laser pulses. The fitting formula is [38]

$$T_{C/O}(x) = 1 + \frac{4x\Delta\Phi}{(1+x^2)(9+x^2)} + \frac{4(3x^2-5)\Delta\Phi^2}{(1+x^2)(9+x^2)(25+x^2)} + \frac{32(3x^2-11)x\Delta\Phi^3}{(1+x^2)(9+x^2)(25+x^2)(49+x^2)}, \quad (3)$$

where $x = z/z_R$, $\Delta\Phi = kn_2I_0L_{\text{eff}}$ is the on-axis nonlinear phase shift at the focus, and k is the wavelength number. Using Eq. (3), we can obtain the nonlinear refractive index n_2 under different conditions. At 355 nm and an input fluence of 0.47 J · cm^{-2}, the n_2 values of g-C_3N_4-1, g-C_3N_4-2, and g-C_3N_4-3 samples are 0.59×10^{-15}, 0.87×10^{-15}, and 1.52×10^{-15} cm^2 · W^{-1}, respectively. For 532 nm excitation, when the input fluence is 1.66 J · cm^{-2}, the n_2 values of

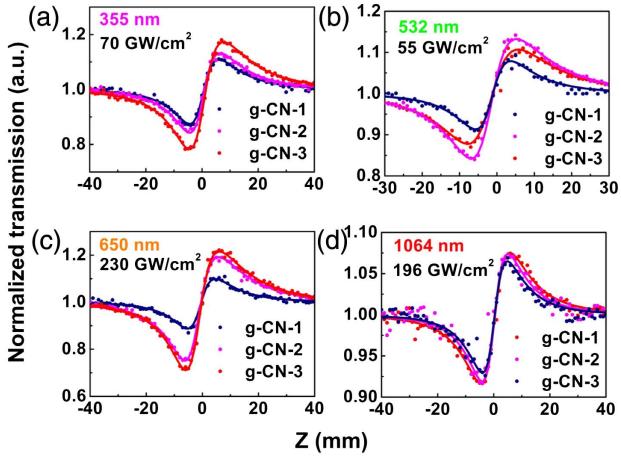

Fig. 8. CA/OA Z-scan results of different g-C_3N_4 samples at (a) 355 nm, (b) 532 nm, (c) 650 nm, and (d) 1064 nm.

g-C_3N_4-1, g-C_3N_4-2, and g-C_3N_4-3 samples are 0.57×10^{-15}, 1.42×10^{-15}, and 1.44×10^{-15} $cm^2 \cdot W^{-1}$, respectively. At 650 nm and an input fluence of 9.23 $J \cdot cm^{-2}$, the n_2 values of g-C_3N_4-1, g-C_3N_4-2, and g-C_3N_4-3 samples are 0.15×10^{-15}, 0.40×10^{-15}, and 0.51×10^{-15} $cm^2 \cdot W^{-1}$, respectively. For 1064 nm excitation, when the input fluence is 7.83 $J \cdot cm^{-2}$, the n_2 values of the three samples are 0.27×10^{-15}, 0.34×10^{-15}, and 0.42×10^{-15} $cm^2 \cdot W^{-1}$, respectively. A high dispersion concentration and short excitation wavelength result in a high nonlinear refractive index.

The imaginary part of the third-order NLO susceptibility, $\mathrm{Im}\chi^{(3)}$, is related to the nonlinear absorption coefficient, and the real part, $\mathrm{Re}\chi^{(3)}$, is related to the nonlinear refractive index. They can be expressed by the following equations [50]:

$$\mathrm{Re}\chi^{(3)}(\mathrm{esu}) = \frac{cn_0^2}{120\pi^2} n_2 \ (\mathrm{m^2/W}), \tag{4}$$

$$\mathrm{Im}\chi^{(3)}(\mathrm{esu}) = \frac{c^2 n_0^2}{240\pi^2 \omega} \beta_2 \ (\mathrm{m/W}), \tag{5}$$

where n_0 is the linear refractive index, and ω is the light frequency. The figure of merit (FOM) for the third-order optical nonlinearity is defined as FOM $= |\mathrm{Im}\chi^{(3)}/\alpha_0|$. The $\mathrm{Re}\chi^{(3)}$, $\mathrm{Im}\chi^{(3)}$, and FOM values of the g-C_3N_4-2 sample are listed in Table 1 for different wavelengths.

4. CONCLUSIONS

g-C_3N_4 nanosheets were fabricated from bulk C_3N_4 by mechanical exfoliation. The nonlinear absorption and nonlinear refractive properties of g-C_3N_4 nanosheets were investigated at the wavelengths of 355, 532, 650, and 1064 nm with the Z-scan technique. For the first time to our knowledge, SA behavior in the visible waveband is observed from g-C_3N_4. At the same time, we found that the SA effect would change to the OL effect with increasing excitation intensity. It indicates that g-C_3N_4 can be used for different applications and be altered depending on the practical working conditions. In summary, this research shows that g-C_3N_4 is an excellent and promising wide waveband NLO material, whose applicable waveband includes the visible region.

Funding. Natural Science Foundation of Shandong Province, China (ZR2017MF031).

†These authors contributed equally to this work.

REFERENCES

1. E. McCann, "Asymmetry gap in the electronic band structure of bilayer graphene," Phys. Rev. B **74**, 161403 (2006).
2. K. S. Novoselov, A. K. Geim, and S. V. Morozov, "Two-dimensional gas of massless Dirac fermions in graphene," Nature **438**, 197–200 (2005).
3. Q. Bao, H. Zhang, and B. Wang, "Broadband graphene polarizer," Nat. Photonics **5**, 411–415 (2011).
4. J. E. Moore, "The birth of topological insulators," Nature **464**, 194–198 (2010).
5. Q. H. Wang, K. Kalantar-Zadeh, and A. Kis, "Electronics and optoelectronics of two-dimensional transition metal dichalcogenides," Nat. Nanotechnol. **7**, 699–712 (2012).
6. G. Zhao, S. Han, and A. Wang, "'Chemical weathering' exfoliation of atom-thick transition metal dichalcogenides and their ultrafast saturable absorption properties," Adv. Funct. Mater. **25**, 5292–5299 (2015).
7. J. Hou, G. Zhao, and Y. Wu, "Femtosecond solid-state laser based on tungsten disulfide saturable absorber," Opt. Express **23**, 27292–27298 (2015).
8. Y. Chen, G. Jiang, and S. Chen, "Mechanically exfoliated black phosphorus as a new saturable absorber for both *Q*-switching and mode-locking laser operation," Opt. Express **23**, 12823–12833 (2015).
9. Z. Zheng, C. Zhao, and S. Lu, "Microwave and optical saturable absorption in graphene," Opt. Express **20**, 23201–23214 (2012).
10. M. Feng, H. Zhan, and Y. Chen, "Nonlinear optical and optical limiting properties of graphene families," Appl. Phys. Lett. **96**, 033107 (2010).
11. Q. Ouyang, K. Zhang, and W. Chen, "Nonlinear absorption and nonlinear refraction in a chemical vapor deposition-grown, ultrathin hexagonal boron nitride film," Opt. Lett. **41**, 1368–1371 (2016).
12. Y. Xie, B. Zhang, and S. Wang, "Ultrabroadband MoS_2 photodetector with spectral response from 445 to 2717 nm," Adv. Mater. **29**, 1605972 (2017).
13. X. Wang, K. Maeda, and A. Thomas, "A metal-free polymeric photocatalyst for hydrogen production from water under visible light," Nat. Mater. **8**, 76–80 (2009).
14. S. Cao, J. Low, and J. Yu, "Polymeric photocatalysts based on graphitic carbon nitride," Adv. Mater. **27**, 2150–2176 (2015).
15. J. Liu, Y. Liu, and N. Liu, "Metal-free efficient photocatalyst for stable visible water splitting via a two-electron pathway," Science **347**, 970–974 (2015).
16. J. Duan, S. Chen, and M. Jaroniec, "Porous C_3N_4 nanolayers@N-graphene films as catalyst electrodes for highly efficient hydrogen evolution," ACS Nano **9**, 931–940 (2015).
17. X. Gao, S. Li, and T. Li, "g-C_3N_4 as a saturable absorber for the passively *Q*-switched Nd:LLF laser at 1.3 μm," Photon. Res. **5**, 33–36 (2017).
18. Y. Zhou, M. Zhao, and S. Wang, "Developing carbon-nitride nanosheets for mode-locking ytterbium fiber lasers," Opt. Lett. **41**, 1221–1224 (2016).
19. M. Fan, T. Li, and G. Li, "Graphitic C_3N_4 as a new saturable absorber for the mid-infrared spectral range," Opt. Lett. **42**, 286–289 (2017).
20. M. Fan, T. Li, and G. Li, "Passively *Q*-switched Ho, Pr:$LiLuF_4$ laser with graphitic carbon nitride nanosheet film," Opt. Express **25**, 12796–12803 (2017).
21. K. Sridharan, T. Kuriakose, and R. Philip, "Transition metal (Fe, Co and Ni) oxide nanoparticles grafted graphitic carbon nitrides as efficient optical limiters and recyclable photocatalysts," Appl. Surf. Sci. **308**, 139–147 (2014).
22. K. Sridharan, P. Sreekanth, and T. J. Park, "Nonlinear optical investigations in nine-atom silver quantum clusters and graphitic carbon nitride nanosheets," J. Phys. Chem. C **119**, 16314–16320 (2015).
23. C. Kränkel, D. T. Marzahl, and F. Moglia, "Out of the blue: semiconductor laserpumped visible rare-earth doped lasers," Laser Photon. Rev. **10**, 548–568 (2016).
24. S. Wang, Y. Zhang, J. Xing, X. Liu, H. Yu, A. Di Lieto, M. Tonelli, T. Sum, H. Zhang, and Q. Xiong, "Nonlinear optical response of Au nanorods for broadband pulse modulation in bulk visible lasers," Appl. Phys. Lett. **107**, 161103 (2015).
25. Y. Zhang, H. Yu, R. Zhang, G. Zhao, H. Zhang, Y. Chen, L. Mei, M. Tonelli, and J. Wang, "Broadband atomic-layer MoS_2 optical modulators for ultrafast pulse generations in the visible range," Opt. Lett. **42**, 547–550 (2017).
26. S. Luo, X. Yan, B. Xu, L. Xiao, H. Xu, Z. Cai, and J. Weng, "Few-layer Bi_2Se_3-based passively *Q*-switched Pr:YLF visible lasers," Opt. Commun. **406**, 61–65 (2018).
27. D. Wu, J. Peng, Z. Cai, J. Weng, Z. Luo, N. Chen, and H. Xu, "Gold nanoparticles as a saturable absorber for visible 635 nm *Q*-switched pulse generation," Opt. Express **23**, 24071–24076 (2015).
28. H. Lin, W. Li, J. Lan, X. Guan, H. Xu, and Z. Cai, "All-fiber passively *Q*-switched 604 nm praseodymium laser with a Bi_2Se_3 saturable absorber," Appl. Opt. **56**, 802–805 (2017).

29. P. Niu, L. Zhang, and G. Liu, "Graphene-like carbon nitride nanosheets for improved photocatalytic activities," Adv. Funct. Mater. **22**, 4763–4770 (2012).
30. Q. Huang, J. Yu, and S. Cao, "Efficient photocatalytic reduction of CO_2 by amine-functionalized g-C_3N_4," Appl. Surf. Sci. **358**, 350–355 (2015).
31. S. Hu, L. Ma, and J. You, "Enhanced visible light photocatalytic performance of g-C_3N_4 photocatalysts co-doped with iron and phosphorus," Appl. Surf. Sci. **311**, 164–171 (2014).
32. S. Tonda, S. Kumar, S. Kandula, and V. Shanker, "Fe-doped and -mediated graphitic carbon nitride nanosheets for enhanced photocatalytic performance under natural sunlight," J. Mater. Chem. A **2**, 6772–6780 (2014).
33. S. Yan, Z. Li, and Z. Zou, "Photodegradation performance of g-C_3N_4 fabricated by directly heating melamine," Langmuir **25**, 10397–10401 (2009).
34. J. Ran, T. Ma, G. Gao, X. Du, and S. Qiao, "Porous P-doped graphitic carbon nitride nanosheets for synergistically enhanced visible-light photocatalytic H_2 production," Energy Environ. Sci. **8**, 3708–3717 (2015).
35. H. Lan, L. Li, X. An, F. Liu, C. Chen, H. Liu, and J. Qu, "Microstructure of carbon nitride affecting synergetic photocatalytic activity: hydrogen bonds vs. structural defects," Appl. Catal. B **204**, 49–57 (2017).
36. M. Sheik-Bahae, A. A. Said, and T. H. Wei, "Sensitive measurement of optical nonlinearities using a single beam," IEEE J. Quantum Electron. **26**, 760–769 (1990).
37. X. Zhang, X. Xie, H. Wang, J. Zhang, B. Pan, and Y. Xie, "Enhanced photoresponsive ultrathin graphitic-phase C_3N_4 nanosheets for bioimaging," J. Am. Chem. Soc. **135**, 18–21 (2012).
38. C. Li, J. Si, and M. Yang, "Excited-state nonlinear absorption in multi-energy-level molecular systems," Phys. Rev. A **51**, 569–575 (1995).
39. X. Deng, X. Zhang, S. Liu, and C. Li, "The theoretical analysis of critical conditions for several nonlinear absorptions," Acta Photon. Sin. **27**, 1077–1090 (1998).
40. N. Liaros, P. Aloukos, A. Kolokithas-Ntoukas, A. Bakandritsos, T. Szabo, R. Zboril, and S. Couris, "Nonlinear optical properties and broadband optical power limiting action of graphene oxide colloids," J. Phys. Chem. C **117**, 6842–6850 (2013).
41. F. Zhang, Z. Wu, Z. Wang, D. Wang, S. Wang, and X. Xu, "Strong optical limiting behavior discovered in black phosphorus," RSC Adv. **6**, 20027–20033 (2016).
42. K. Zhou, M. Zhao, M. Chang, Q. Wang, X. Wu, Y. Song, and H. Zhang, "Size-dependent nonlinear optical properties of atomically thin transition metal dichalcogenide nanosheets," Small **11**, 694–701 (2015).
43. F. Zhang, Z. Wang, D. Wang, Z. Wu, S. Wang, and X. Xu, "Nonlinear optical effects in nitrogen-doped graphene," RSC Adv. **6**, 3526–3531 (2016).
44. Z. Liu, Y. Wang, X. Zhang, Y. Xu, Y. Chen, and J. Tian, "Nonlinear optical properties of graphene oxide in nanosecond and picosecond regimes," Appl. Phys. Lett. **94**, 021902 (2009).
45. A. B. Bourlinos, A. Bakandritsos, N. Liaros, S. Couris, K. Safarova, M. Otyepka, and R. Zbořil, "Water dispersible functionalized graphene fluoride with significant nonlinear optical response," Chem. Phys. Lett. **543**, 101–105 (2012).
46. F. Ma, M. Wang, and Y. Shao, "Thermal substitution for preparing ternary BCN nanosheets with enhanced and controllable nonlinear optical performance," J. Mater. Chem. C **5**, 2559–2565 (2017).
47. U. Keller, "Recent developments in compact ultrafast lasers," Nature **424**, 831–838 (2003).
48. Z. Chen, Q. Zhang, and Y. Luo, "Determining the charge-transfer direction in a p-n heterojunction BiOCl/g-C_3N_4 photocatalyst by ultrafast spectroscopy," ChemPhotoChem **1**, 350–354 (2017).
49. J. Wang, Y. Hernandez, and M. Lotya, "Broadband nonlinear optical response of graphene dispersions," Adv. Mater. **21**, 2430–2435 (2009).
50. G. Yang, W. Wang, and L. Yan, "Z-scan determination of the large third-order optical nonlinearity of Rh: $BaTiO_3$ thin films deposited on MgO substrates," Opt. Commun. **209**, 445–449 (2002).